RSC Advances

ROYAL SOCIETY OF CHEMISTRY

www.rsc.org/advances

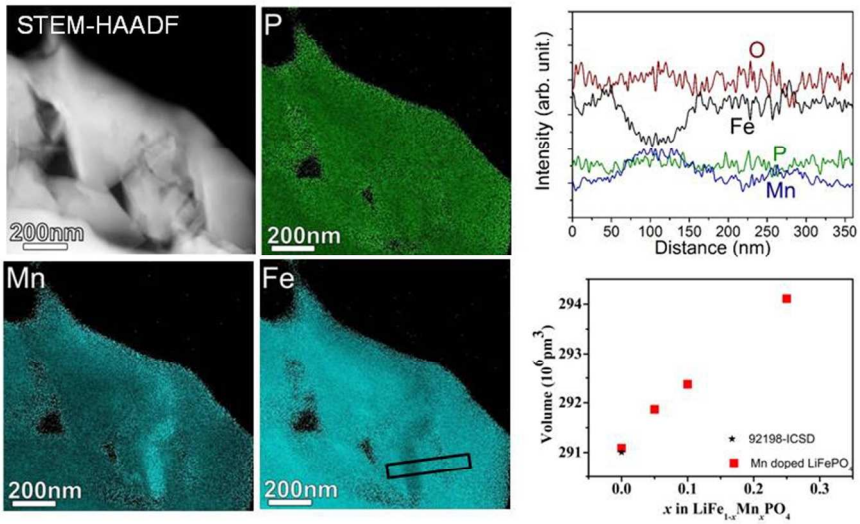

Mn-rich nano-scale secondary phase were identified in $LiFe_{1-x}Mn_xPO_4$, despite of known complete solubility for $LiFePO_4$-$LiMnPO_4$ system and observed linear increase in the lattice parameters of $LiFe_{1-x}Mn_xPO_4$ with increasing Mn concentration

254x190mm (96 x 96 DPI)

Raman spectral signature of Mn-rich nanoscale phase segregations in carbon free $LiFe_{1-x}Mn_xPO_4$ prepared by hydrothermal technique

M.B. Sahana, S. Vasu, N. Sasikala, S. Anandan, and R. Gopalan

Centre for Automotive Energy Materials , International Advanced Research Centre for Powder Metallurgy and New Materials , IITM Research Park, Chennai-600113, India

H. Sepehri-Amin

National Institute for Materials Science, 1-2-1 Sengen, Tsukuba, Ibaraki, 305-0047 Japan

C. Sudakar

Multifunctional Materials Laboratory, Department of Physics, Indian Institute of Technology Madras, Chennai 600036, India

Abstract

Mn-rich nanoscale secondary phases were identified in $LiFe_{1-x}Mn_xPO_4$, despite of known complete solubility for $LiFePO_4$-$LiMnPO_4$ system and observed linear increase in the lattice parameters of $LiFe_{1-x}Mn_xPO_4$ with increasing Mn concentration. Carbon free $LiFe_{1-x}Mn_xPO_4$ (x = 0, 0.05, 0.10, 0.25) were prepared by sequential precipitation of Li_3PO_4 and $(Fe_{1-x}Mn_x)_3(PO_4)_2$ followed by hydrothermal treatment. At low doping concentration ($x \leq 0.05$), Li-Mn-O secondary phases were discerned by Raman spectra, which corroborates with the inductively coupled plasma elemental analysis. Though, energy dispersive elemental mapping with scanning transmission electron microscopy do not show segregation of Mn at low concentrations, Mn-rich phases were clearly discerned at high doping concentration (x = 0.25). The kinetics of Mn rich phase formation during hydrothermal synthesis of carbon free $LiFe_{1-x}Mn_xPO_4$, which was attributed to the difference in the solubility constant of the intermediate products of Li_3PO_4 and

$(Fe_{1-x}Mn_x)_3(PO_4)_2$, and its implications on the capacity of $LiFe_{1-x}Mn_xPO_4$ cathode material were discussed. Our results present how de-convoluted Raman peaks show clear signatures of nano phase impurity segregations and increase in the lattice constant with Mn doping concentration can be decisive.

Key words: Raman spectroscopy; STEM, Impurity segregation, Phase separation, $LiFe_{1-x}Mn_xPO_4$

1. Introduction:

Phospho-olivines ($LiMPO_4$; M= Fe, Mn, Co) and its doped derivatives are intensively studied due to their application as cathodes in lithium ion batteries for electric and hybrid electric vehicles. $LiMPO_4$ structure has good thermal and chemical stability.[1] However, one of the main limitations of these compounds is its low intrinsic electronic conductivity (< 10^{-9} S/cm) and low Li-ion diffusion coefficient (10^{-11} to 10^{-13} cm^2s^{-1}) which hinders its application in high power batteries.[2] To circumvent these drawbacks, several approaches including carbon coating, reduction in particle size, doping with other transition metals have been extensively explored.[1, 3]

Mixed metal solid solution of olivine compounds is one such possibility which can considerably enhance the electrochemical characteristics such as power density and specific capacity.[4] Recently significant research activities exploring various combinations of metal cations in $LiMPO_4$ are being reported.[5] The main focus of such studies includes finding compounds with an optimized electrochemical properties similar to the studies on the optimization of layered compounds [5a] which led to the famous $LiMn_{1/3}Co_{1/3}Ni_{1/3}O_2$ (1/3 1/3 1/3) cathode materials.[6] $LiFe_{1-x}Mn_xPO_4$ is one of the various solid solutions that is being considered as potential cathode material.[7] The possible enhancement in the mobility of lithium along the *b*-axis in low concentration Mn doped $LiFePO_4$, is attributed to widening of 1D-channels along the *b*-axis and increase in the diffusion coefficient.[8] The local distribution of cations in olivine structure, therefore, is very crucial in determining the electrochemical properties. The phospho-olivine structure of $LiMPO_4$ (M= Fe, Mn, Co,) is made up of hexagonally close packed oxygen arrays in which transition metal ions occupy corner-shared M2 octahedral site, lithium ions occupy edge-shared M1 octahedral site and phosphorus ions are located in tetrahedral sites.[9] Li-ion diffusion is energetically favored along *b*-axis (i.e. 1D transport) and can be hindered due to

the blockage of 1D pathway by the presence of defects and impurities.[10] Further, formation of Mn rich impurity phases can hamper the diffusion of lithium ions. These structural factors are significantly influenced by the synthesis method.[11]

$LiFePO_4$ and its derivatives have been synthesized by various solid state and wet chemical techniques. Among these, hydrothermal method is considered as economical and viable for large scale production. A review on the synthesis of phospho-olivine compounds is reported by Jugović*et.al.* [11] It has been found that hydrothermal process parameters such as temperature, duration, pH of the solution, starting chemicals and the sequence of mixing greatly influence the microstructure, defects, impurities, and local structural features, which in turn affect the electrochemical characteristics.[11] In majority of the structural studies on $LiFe_{1-x}Mn_xPO_4$, Mn substitution at Fe site has been shown by systematic increase in the lattice parameters.[12] However, the presence of Fe_{Li} anti-site defect (excees Fe occupying Li site) is shown to be frozen-in due to the Mn substitution and does not seem to get removed even at high temperature or extended annealing conditions.[13] Furhter, solvothermal preparation of $LiFe_{1-x}Mn_xPO_4$ is shown to contain mixed phases of $LiFePO_4$ and $LiMnPO_4$ instead of $LiFe_{1-x}Mn_xPO_4$ solid solution.[14] While the presence of defects or phase segregation can be investigated using state-of-the-art sophisticated characterization techniques, the same cannot be used in quality control for the mass production. Also, when secondary phases exist in very small quantity or in an amorphous form it is a challenging task to identify the secondary phases present. A combination of characterization techniques such as FTIR and Raman spectra, magnetometry, elemental mapping,[15] and overall elemental concentration as identified by inductively coupled plasma[16] are required in identifying the secondary phases.[17]

In this report we present the effect of Mn doping on the structural properties of $LiFePO_4$ synthesized by hydrothermal technique. Despite the observation of linear increase in the lattice parameter with Mn substitution we show by using Raman and Fourier transform infrared spectroscopy the signatures of Mn-rich secondary phases [Li_2MnO_3 or $LiMnO_2$ and $Mn_3(PO_4)_2$] in $LiFe_{1-x}Mn_xPO_4$, which is further substantiated by several techniques including x-ray diffraction (XRD), magnetometry, inductively coupled plasma - optical emission spectrometry (ICP-OES), high-resolution transmission electron microscopy (HRTEM) and scanning transmission electron microscope-energy dispersive spectroscopy (STEM-EDS) elemental mapping. These Mn-rich phases are identified in small concentration as nano-sized impurity phases present within the crystalline lattice of hydrothermally synthesized $LiFe_{0.75}Mn_{0.25}PO_4$. We further discuss the implications of such Mn-rich inclusions on the electrochemical properties.

2. Experimental:

Co-precipitation or sequential precipitation methods are commonly used to prepare multicomponent phases. In this study, we used a sequential method by beginning with the required ratio of metal cation to anions in the final component. Carbon free $LiFe_{1-x}Mn_xPO_4$ (x = 0, 0.05, 0.1, 0.25) was synthesized by hydrothermal technique using chemicals $LiOH.H_2O$, $FeSO_4.7H_2O$, $(NH_3)_2HPO_4$ and $MnSO_4.H_2O$. Aqueous $(NH_3)_2HPO_4$ solution (1M) was added to aqueous solution of $LiOH.H_2O$ (1M) under constant stirring under N_2 ambient giving rise to a white precipitate. To this white precipitate, 1 M solution mixture of $x FeSO_4.7H_2O$ + (1-x) $MnSO_4.H_2O$ was added which resulted in the formation of a green colored thick gel. The pH of the final solution was 7.5 and after stirring for 30 minutes, the homogenous solution was transferred to a Teflon autoclave and heated for 10 h at 200 °C. The precipitate formed after

hydrothermal treatment was filtered and washed several times with de-ionized water until it was free of sulphate ions. The final filtrates were dried under vacuum in a desiccator. For this study four samples of $LiFe_{1-x}Mn_xPO_4$ with different Mn concentration, x=0, 0.05, 0.1, 0.25, were synthesized and further characterized for structural properties. The phase formation in as-prepared samples was confirmed by x-ray powder diffractometer (X'pert-Pro, PANalytical) with a 1.2 kW Cu K_α (λ = 1.5406 Å). To understand the effect of Mn doping on formation of the impurity phases, Fourier transfer infrared spectroscopy (FTIR) was taken using Perkin-Elmer spectrometer (Spectrum One) in the range from 400 to 4000 cm^{-1} after dispersing the samples in anhydrous KBr pellet. Further the presence of impurities was studied using Raman spectroscopy (Horiba Jobin-Yvon, HR 800UV) in the range between 200 to 1500 cm^{-1} using 488 nm Ar^+-ion laser source. The magnetic behavior of the samples were studied using a physical property measurement unit (PPMS, Quantum Design) operating under the VSM mode. The isothermal magnetization studies were carried out with a magnetic field varying in the range of +7 to -7 T. The susceptibility studies with constant magnetic field were studied from 5K to 300K. Elemental analyses were carried out using ICP-OES. The morphology of the prepared samples was observed using a Hitachi S-4300 field emission scanning electron microscope (FE-SEM, Hitachi Co. Ltd. S-4300) operating at 20 KV. To prevent charging of the samples, the samples were coated with a thin gold layer by sputtering process for 1 min. Transmission electron microscopy (TEM) was performed using a Technai G2 F30 TEM and a Titan G2 80-200 TEM with a probe corrector. Energy dispersive X-ray spectroscopy (EDS) was conducted in Titan G2 80-200 TEM using a Super-X EDX detector. EDS maps were constructed using Fe-K_α, Mn-K_α, O-K_α, and P-K_α. For electrochemical characterization, the cathodes were prepared by mixing active material, acetylene Black as a conducting carbon, and polyvinylidene fluoride as binder at

a weight ratio of 80 : 10 : 10, respectively, using *N*-methyl pyrrolidone solvent. The resulting slurry was coated uniformly on Al foil and dried 120 °C for 12 h and disk electrodes were cut. Coin cells with lithium as counter electrode were fabricated in argon filled glove box with less than 1 ppm oxygen and moisture. 1 M $LiPF_6$ was used as electrolyte dissolved in ternary solvent, ethylene carbonate (EC) and dimethyl carbonate (DMC) with the ratio of 50:50. Galvanostatic charge and discharge studies were performed at a current of 0.1 mA with cut off voltages of 2.2–4.4 V at room temperature using Arbin instruments (Model: BT2000)

3. Results:

Figure 1 shows the morphology of $LiFe_{1-x}Mn_xPO_4$ (x= 0, 0.05, 0.1, 0.25) samples studied by FESEM. All the samples showed well faceted, oriented crystallites with uniform size distribution. The XRD of as prepared carbon free $LiFe_{1-x}Mn_xPO_4$ (x=0, 0.05, 0.1, 0.25) powder samples (Fig. 2a) reveals the formation of phospho-olivine phase where all the peaks were indexed according to the standard ICDD pattern 98-003-5125. The lattice parameters and the unit cell volume show a linear increase with Mn doping concentration as shown in Fig.2b which was in accordance to the reported change in lattice parameters with Mn doping.[12] Few of the very low intensity peaks at 2θ=14.6°, 25.32°, 31.76°, and 35.09° seen clearly in x=0 sample correspond to the sarcopside phase of $Fe_3(PO_4)_2$. This sarcopside phase [18] is equivalent to phospho-olivine with no Li cations. Further, one half of the Li sites (M1) in phospho-olivine structure is occupied by Fe or other ions of the transition metal such as Mn, Cr, Co and the other half of M1 site is vacant, *i.e.* $M_3(PO_4)_2$ can be visualized as $M_{0.5}MPO_4$ (M= Fe, Mn, Cr, etc). With Mn doping and increase in the concentration of Mn substitution, no noticeable changes in the intensity of XRD peaks corresponding to sarcopside [$Fe_3(PO_4)_2$/ $(Fe_{1-y}Mn_y)_3PO_4$, $x \neq y$] was observed. The discharging capacity (not shown) of $LiFe_{1-x}Mn_xPO_4$ were found to be approximately 60 mAh/g,

which is low compared to the theoretical capacity of $LiFePO_4$ (170 mAh/g) at 0.1C rate. It should be noted, in general, that due to poor electronic and ionic conductivity of phospho-olivine compounds the capacity exhibited by the cathode will be lower than theoretical capacity. This is generally improved by substantial size reduction and achieving proper conductive coating on the nanoparticles. In our samples the particle size was large (~1 μm) and there was no carbon coating. However, to understand and address phase-segregation related decrease in capacity of $LiFe_{1-x}Mn_xPO_4$ various structural characterizations were carried out. To investigate the presence of possible amorphous phases and lithium deficiency, ICP-OES was carried out and the Li:Fe:Mn:P ratio for these samples are listed in Table I. Elemental analysis of undoped $LiFePO_4$ sample suggests that compared to the stochiometric $LiFePO_4$, the sample consists an excess 18 *at.*% of phosphor and an excess of 24 *at.*% of iron with respect to lithium. This excess concentration of Fe and P corresponds to ~10 mol % of $Fe_3(PO_4)_2$ in $LiFePO_4$. However, very low intensity of $Fe_3(PO_4)_2$ peaks in XRD indicates that not all excess Fe and P will exist as $Fe_3(PO_4)_2$, and part of the excess Fe can also reside at the Li site in $LiFePO_4$. With the incorporation of Mn, though phosphor concentration decreases, there was no change in the Li concentration, suggesting the formation Li-Mn-O phases. The absence of any x-ray reflections corresponding to Li-Mn-O phases suggests possible presence of the amorphous phase or very low concentration of nanocrystalline Li-Mn-O phases.

Magnetometric measurements [19] were carried out to detect the presence of small concentration of magnetic impurities like Fe_2P or Fe_2O_3. Figure 3(a-b) shows the temperature dependent inverse magnetic susceptibility of $LiFe_{1-x}Mn_xPO_4$ samples depicting the antiferromagnetic-paramagnetic transition with Néel temperature around 50±2K. The μ_{eff} calculated from paramagnetic region [17b] of χ^{-1} *vs* temperature plot is given in Table II. Mn

substitution in $LiFePO_4$ increases μ_{eff} from 5.3 μ_B to 5.8 μ_B. The change in μ_{eff} is similar to the trend reported by Yamada *et. al.*[17b] suggesting the contribution from spin and angular momentum. The temperature dependent magnetic susceptibility reveals the absence of magnetic transitions due to the other phases, especially the antiferromagnetic transition at ~120 K characteristics of FeP and a ferromagnetic transition at ~265 K of Fe_2P impurities. This confirms that the hydrothermally synthesized $LiFe_{1-x}Mn_xPO_4$ are free from FeP and Fe_2P impurities [20]. Absence of the magnetic impurities like Fe_2P or γ-Fe_2O_3 was further confirmed by the linear dependence of magnetization on magnetic field measured at various temperatures (Fig.3c).

Though the XRD patterns and magnetometry analyses suggests close to phase pure nature of the $LiFe_{1-x}Mn_xPO_4$ sample except for $(Fe_{1-x}Mn_x)_3PO_4$, the compositional analyses shows significant offset from the expected Li:Fe:Mn:P stoichiometry. This indicates the presence of other possible impurity phases mainly comprising of amorphous or nanocrystalline forms of Li-Mn-O phase. Raman spectroscopy can be used to identify such phases as it is very sensitive down to the molecular level (Fig. 4). However, one should be cautious and aware of the decomposition of $LiFePO_4$ due to laser heating and therefore posing a challenge to the phase analysis [21]. In this study we used 488 nm laser with a power density of 1 mW/20 μm^2 to avoid the decomposition of sample while acquiring the spectra and further ascertained all the vibrations were characteristics of the $LiFe_{1-x}Mn_xPO_4$ sample investigated. Since the relative intensity of Raman spectral modes at ~ 950 cm^{-1} is very high, and the features below 800 $cm^{-1}$are small, for clarity the Raman spectra of $LiFe_{1-x}Mn_xPO_4$ from wavenumber 100 to 800 cm^{-1} and 800 to 1300 cm^{-1} are given in separate figures Fig.4a and Fig.4b respectively. A vibrational spectrum of $LiFePO_4$ is generally classified into internal modes corresponding to vibrations in the range 400 to 1200 cm^{-1} and external modes from 100 to 400 cm^{-1}. The relative intensity of the vibrational

features match with Raman spectral data reported by *Paraguassu et. al.*[22], and there was no discernible changes due to Mn substitution in $LiFePO_4$ in the external modes of vibration. However, we observe clear influence of Mn doping on internal modes which originate due to the intramolecular vibrations of the PO_4^{3-} polyanions. To see this effect, the bending modes of PO_4^{3-} peaks are fitted to mixed Gaussian and Laurentian shape profiles and the corresponding fitted plots in the range from 400 to 700 $cm^{-1}$are given in Fig.4c. The broad mode appearing at ~ 440 cm^{-1}can be fitted into two distinct peaks for pure $LiFePO_4$, however a best fit in Mn doped $LiFePO_4$ could be obtained with either 3 or 4 peaks. The vibrational mode at 405 $cm^{-1}$is attributed to external mode of $LiFePO_4$, whereas the mode at ~440 cm^{-1} is due to the overlapping bending modes of $LiFePO_4$. The Raman bands at 573, 591 and 629 cm^{-1} are due to bending modes of PO_4^{3-}. From the fitted peak it is evident that the intensity of the Raman signal at 556 cm^{-1} (shown with arrow) increases with Mn concentration. We attribute the additional bands at 426 and 556 cm^{-1}, that are observed only with Mn substitution in $LiFePO_4$, to vibrations corresponding Li-Mn-O phases [23]. Although it is difficult to comment on the specific phase that give rises to these vibrational modes, such modes are characteristics of Li-Mn-O phases as reported in the literature [24]. The Raman spectra of pure and Mn substituted $LiFePO_4$ samples in the range of 900 to 1200 cm^{-1}, have a strong peak at ~ 947 cm^{-1} due to symmetric stretching mode, and peaks 997 and 1066 cm^{-1} due to asymmetric stretching mode of PO_4^{3-}. The low intensity shoulder peaks at 926 and 971 cm^{-1}, whose relative intensity increases with increasing in Mn concentration, are attributed to modes from $Fe_3(PO_4)_2$/ $Mn_3(PO_4)_2$/$(Fe_{1-x}Mn_x)_3PO_4$ [25].

The IR spectral modes of $LiFePO_4$ have been reported to show a significant shift in the stretching and bending modes of PO_4^{3-} due to the presence of Fe_{Li} antisite defects[26]. Such Fe_{Li} antisite defects which accommodate Li deficiency have been more commonly reported in the

hydrothermally prepared $LiFePO_4$ samples. The Li deficiency found from ICP analysis of $LiFe_{1-x}Mn_xPO_4$ also signify the possible presence of such of Fe_{Li} antisite defects. To investigate how $LiFe_{1-x}Mn_xPO_4$ accommodates lower atomic concentration of Li from stoichiometric $LiFePO_4$ and low Li and P atomic concentration in Mn doped $LiFePO_4$, FTIR spectroscopy of these samples were carried out (Fig.5a). The positions of the vibrational modes of all $LiFe_{1-x}Mn_xPO_4$ matches well with reported values [26]. We did not find any change in the vibrational modes in FTIR spectra except for small increase in the $\nu_1$vibrational mode positions with increase in the Mn concentration. As depicted in Fig.5c, ν_1 mode can be resolved in to two bands, one ~ 960 cm^{-1} and the second ~972 cm^{-1}. A shift to high frequency of these band was observed with increase in Mn concentration, which is probably due to increase in the Fe_{Li} antisite defect concentration[26]. Shifting of the vibration bands to higher frequency has been reported earlier by Bini *et. al.* [27] with Mn substitution in $LiFePO_4$.

To investigate the local structural details and elemental distribution, we carried out HRTEM and STEM-EDS elemental mapping analysis. The representative bright field image, HRTEM and elemental mappings are shown in Figs. 6 and 7 for $LiFe_{1-x}Mn_xPO_4$ samples with x=0.05 and x=0.25 respectively. The HRTEM image of one of the crystallites is shown in Fig. 6b. The compositional analyses studied by the EDS-mapping clearly depict the homogeneous distribution of all the elements across the crystal (Fig. 6(d) in $LiFe_{0.95}Mn_{0.05}PO_4$. However, STEM investigations of $LiFe_{0.75}Mn_{0.25}PO_4$, reveals Mn rich regions within the crystalites. The aerial mapping of Fe, Mn, P and O elements of a part of a crystalite is shown in Fig. 7(d) depicting Mn rich region of ~ 50 nm. It should be noted at this region, though there was decrease in Fe concentration, phosphor concentration is uniform throughout the crystal. The line-profile obtained from the region marked in Fig. 7(d) is given in Fig. 7(c) and shows clearly the

local elemental variations leading to Mn-rich regions with in the $LiFe_{1-x}Mn_xPO_4$ crystals. These local structural and elemental characterisation obtained from STEM-EDS mapping substantiate the observations from Raman and FTIR that with increasing Mn concentration in $LiFePO_4$, the Mn rich nanoscale phase precipitates within $LiFe_{1-x}Mn_xPO_4$ phase.

4. Discussion:

From the above studies, it is clear that hydrothermal conditions and sequential precipitation conditions that were used in this study, also favors the formation of small concentration of Li-Mn-O and nanosized Mn rich sarcopside phase segregation within the lattice of $LiFe_{1-x}Mn_xPO_4$. Therefore it is evident from the IR, Raman and STEM investigations of $LiFe_{1-x}Mn_xPO_4$ that even when there is an increase in the lattice constant with Mn concentration, the presence of impurity phases or segregation of secondary phases within the lattice of $LiFePO_4$ shouldn't be ruled out.

In the sequential precipitation of $LiFe_{1-x}Mn_xPO_4$, when $(NH_3)_2HPO_4$ is added to LiOH, the pH was 11 and under this pH, Li_3PO_4 was precipitated as surmised from its white color [12, 14]. Addition of Fe precursor to this mixture reduces the pH to 7.5 and favors the formation of $Fe_3(PO_4)_2$ along with Li_3PO_4 with the molecular level mixing of these two phases in gel form. In earlier investigations using sequential precipitation method, an excess Li molar ratio, three times higher than PO_4 concentration, was used [28]. Due to this, PO_4^{3-} anions were almost completely utilized for the formation of Li_3PO_4, and only very small quantity of $Fe_3(PO_4)_2$ was formed when Fe^{2+} solution was added. The concentration of Li_3PO_4 and $Fe_3(PO_4)_2$ is governed by the solubility limit of the two product. The solubility product (K_{sp}) at room temperature is of the order of 1.0×10^{-36} $mol^5\ l^{-5}$ for $Fe_3(PO_4)_2$ which is much smaller than 3.2×10^{-9} $mol^4\ l^{-4}$ for

Li_3PO_4, therefore formation of $Fe_3(PO_4)_2$ is preferred to that of Li_3PO_4 [11, 28]. In the present investigation, in contrast to earlier study, equal concentration of Li, Fe, and P were used, and therefore it is expected to have molecular level mixture of both $Fe_3(PO_4)_2$ and Li_3PO_4 in as prepared precipitate. The formation of $LiFePO_4$ from $Fe_3(PO_4)_2$ can be understood from the close structural similarities between $LiFePO_4$ and $Fe_3(PO_4)_2$.The detailed crystal structure similarities are discussed by Moore [19b]. The two structures can be visualized as made up of hexagonal close packing of oxygen. In $LiFePO_4$ the M2 octahedral sites are occupied by Fe and M1 octahedral sites are occupied by Li and tetrahedral sites correspond to PO_4. The anology of Fe_3PO_4 structure of sarcopside with olivine $LiFePO_4$ can be visualized, by writing $Fe_3(PO_4)_2$ as $Fe_{0.5}FePO_4$. In sarcopside, half of the M2 sites are occupied by 0.5 Fe atoms leaving half of the M2 sites empty compared to the olivine phase, and remaining Fe occupies M1 site and P occupies tetrahedral site, very similar to olivine phase. The unit cell lattice parameters are also very close to each other. Therefore the only difference in the structure of olivine and sarcopside is the occupation of M2 sites. During hydrothermal synthesis, due to larger solubility product, Li_3PO_4 dissociates to Li^+ and $(PO_4)^{3-}$,and Li migrates to empty M2 site of sarcopside and also partially replace remaining Fe in M2 sites of $Fe_3(PO_4)_2$ to form $LiFePO_4$. Thus the reduction in the Li^+ concentration in the solution further drives the dissociation of Li_3PO_4. However, it appears that complete replacement of Fe in M1 site by Li does not take place, which results in the presence of small fraction of $Fe_3(PO_4)_2$ in the final product. This also leads to a significant loss of Li (~ 25 *at.*%) and P (~ 5 *at.* %) as identified by ICP-OES [14].

In $LiFe_{1-x}Mn_xPO_4$ sequencial precipitations, similar to $LiFePO_4$ preparation 1 M solution of $(NH_3)_2HPO_4$ was added to 1 M solution of LiOH to form Li_3PO_4. To this mixture, when Mn and Fe precursors are introduced, $(Fe_{1-x}Mn_x)_3(PO_4)_2$ was formed along with Li_3PO_4 and these

two products react to give $LiFe_{1-x}Mn_xPO_4$ during the hydrothermal treatment. It was observed by ICP analysis that in Mn substituted samples, though Li concentration remains the same as that of undoped $LiFePO_4$, phosphor concentration decreases drastically. This can be understood from the slightly higher solubility product of $Mn_3(PO_4)_2$ [1x 10^{-27} mol^5 l^{-5}] than that of $Fe_3(PO_4)_2$ and smaller than Li_3PO_4. When Mn is also present along with Fe, Li gets incorporated into $(Fe_{1-x}Mn_x)_3(PO_4)_2$ leading to $LiFe_{1-x}Mn_xPO_4$, very similar to $LiFePO_4$. At high concentration this also leads to local precipitation of Mn rich regions, probably $Mn_3(PO_4)_2$ as within the phopho-olivine phase as discerned from STEM studies and further substantiated by Raman and FTIR spectral studies. The dissolved Mn, P, and Li ions in the hydrothermal solutions also favor the precipitation of small concentration of Li-Mn-O, which are identified by Raman and IR spectroscopy. The segregation of the secondary phases within the lattice of $LiFePO_4$ hinders the intercalation and deintercalation of Li^+ through the lattice.

5. Conclusions:

Carbon free $LiFe_{1-x}Mn_xPO_4$(x = 0, 0.05, 0.1, 0.25) is synthesized using hydrothermal treatment of Li_3PO_4 and $(Fe_{1-x}Mn_x)_3(PO_4)_2$ gel obtained by sequential addition of Fe to Li and P solution in Li: Fe: P ratio of 1: 1: 1. Predominantly phase pure $LiFe_{1-x}Mn_xPO_4$ is obtained as evidenced from XRD. However very dilute concentration of the Mn rich impurity phases [Li-Mn-O and $(Fe_{1-y}Mn_y)_3(PO_4)_2$] are discerned by FTIR, Raman spectroscopy and elemental analysis by ICP. These Mn rich regions are clearly shown to exist as nanoscale segregations within the lattice of $LiFe_{1-x}Mn_xPO_4$for x = 0.25. It is difficult to identify the nanoscale segregation from XRD and TEM at low Mn concentrations, but the signature of these can be identified from FTIR and Raman spectroscopy. Such nanoscale lattice segregations in $LiFe_{1-x}Mn_xPO_4$ can arise during hydrothermal process, wherein Li from Li_3PO_4 diffuse into structurally similar phopho-olivine

like $(Fe_{1-x}Mn_x)_3(PO_4)_2$ lattice. Formation of the $LiFe_{1-x}Mn_xPO_4$ from $(Fe_{1-x}Mn_x)_3(PO_4)_2$ can further be understood in terms of the difference in the solubility limits of constituents and crystal structure similarities between $LiFe_{1-x}Mn_xPO_4$ from $(Fe_{1-x}Mn_x)_3(PO_4)_2$. The nanoscale lattice segregations and associated localized disorder in $LiFe_{1-x}Mn_xPO_4$ will significantly affect the Li diffusion coefficient and charge capacity in the electrochemical properties.

Acknowledgement: We would like to thank the financial support received from the Department of Science and Technology, (DST-SERC) Government of India (No. 1R/S3/EU/0001/2011). The authors are thankful to Director, ARCI for his constant encouragement and discussion during the course of this work. Te authors would like to acknowledge Dr. Ranjith Ramadurai, IIT Hyderabad, for the magnetic measurements and Prof. K. Hono, Director, Magnetic Materials Unit, National Institute for Materials Science for extended TEM-STEM characterization facilities.

Table I: The compositional analyses of $LiFe_{1-x}Mn_xPO_4$ samples from ICP-OES analyses.

Nominal composition of the Sample	Elemental concentration from ICP-OES			
	Li	**Fe**	**Mn**	**P**
$LiFePO_4$	0.76	1	0	0.94
$LiFe_{0.95}Mn_{0.05}PO_4$	0.67	0.92	0.08	0.56
$LiFe_{0.90}Mn_{0.1}PO_4$	0.73	0.85	0.15	0.58
$LiFe_{0.75}Mn_{0.25}PO_4$	0.65	0.72	0.28	0.55

Table II: Neel temperature and effective magnetic moment of $LiFe_{1-x}Mn_xPO_4$ samples

x in $LiFe_{1-x}Mn_xPO_4$	T_N (K)	μ_{eff}
0	50.55	5.32 μ_B
0.5	53.07	5.70 μ_B
0.10	52.35	5.62 μ_B
0.25	50.87	5.77 μ_B

References

1. Zhang, W.-J., Structure and performance of LiFePO4 cathode materials: A review. *Journal of Power Sources* **2011,** *196* (6), 2962-2970.
2. Tang, X. C.; Li, L. X.; Lai, Q. L.; Song, X. W.; Jiang, L. H., Investigation on diffusion behavior of Li+ in LiFePO4 by capacity intermittent titration technique (CITT). *Electrochimica Acta* **2009,** *54* (8), 2329-2334.
3. Yuan, L.-X.; Wang, Z.-H.; Zhang, W.-X.; Hu, X.-L.; Chen, J.-T.; Huang, Y.-H.; Goodenough, J. B., Development and challenges of LiFePO4 cathode material for lithium-ion batteries. *Energy & Environmental Science* **2011,** *4* (2), 269-284.
4. Hautier, G.; Jain, A.; Chen, H.; Moore, C.; Ong, S. P.; Ceder, G., Novel mixed polyanions lithium-ion battery cathode materials predicted by high-throughput ab initio computations. *Journal of Materials Chemistry* **2011,** *21* (43), 17147-17153.
5. (a) Muraliganth, T.; Manthiram, A., Understanding the Shifts in the Redox Potentials of Olivine LiM1−yMyPO4 (M = Fe, Mn, Co, and Mg) Solid Solution Cathodes. *The Journal of Physical Chemistry C* **2010,** *114* (36), 15530-15540; (b) Malik, R.; Zhou, F.; Ceder, G., Phase diagram and electrochemical properties of mixed olivines from first-principles calculations. *Physical Review B* **2009,** *79* (21), 214201; (c) Molenda, J.; Kulka, A.; Milewska, A.; Zając, W.; Świerczek, K., Structural, Transport and Electrochemical Properties of LiFePO4 Substituted in Lithium and Iron Sublattices (Al, Zr, W, Mn, Co and Ni). *Materials* **2013,** *6* (5), 1656-1687; (d) Seo, D.-H.; Gwon, H.; Kim, S.-W.; Kim, J.; Kang, K., Multicomponent Olivine Cathode for Lithium Rechargeable Batteries: A First-Principles Study. *Chemistry of Materials* **2009,** *22* (2), 518-523.
6. (a) Park, Y.-U.; Kim, J.; Gwon, H.; Seo, D.-H.; Kim, S.-W.; Kang, K., Synthesis of Multicomponent Olivine by a Novel Mixed Transition Metal Oxalate Coprecipitation Method and Electrochemical Characterization. *Chemistry of Materials* **2010,** *22* (8), 2573-2581; (b) Gwon, H.; Seo, D.-H.; Kim, S.-W.; Kim, J.; Kang, K., Combined First-Principle Calculations and Experimental Study on Multi-Component Olivine Cathode for Lithium Rechargeable Batteries. *Advanced Functional Materials* **2009,** *19* (20), 3285-3292; (c) Nam, K.-W.; Wang, X.-J.; Yoon, W.-S.; Li, H.; Huang, X.; Haas, O.; Bai, J.; Yang, X.-Q., In situ X-ray absorption and diffraction studies of carbon coated LiFe1/4Mn1/4Co1/4Ni1/4PO4 cathode during first charge. *Electrochemistry Communications* **2009,** *11* (4), 913-916.
7. Kim, J.; Park, K.-Y.; Park, I.; Yoo, J.-K.; Hong, J.; Kang, K., Thermal stability of Fe-Mn binary olivine cathodes for Li rechargeable batteries. *Journal of Materials Chemistry* **2012,** *22* (24), 11964-11970.
8. Lee, K. T.; Lee, K. S., Electrochemical properties of LiFe0.9Mn0.1PO4/Fe2P cathode material by mechanical alloying. *Journal of Power Sources* **2009,** *189* (1), 435-439.
9. Padhi, A. K.; Nanjundaswamy, K. S.; Goodenough, J. B., Phospho-olivines as Positive-Electrode Materials for Rechargeable Lithium Batteries. *Journal of The Electrochemical Society* **1997,** *144* (4), 1188-1194.

10. Fisher, C. A. J.; Prieto, V. M. H.; Islam, M. S., Lithium battery materials LiMPO4 (M = Mn, Fe, Co, and Ni): Insights into defect association, transport mechanisms, and doping behavior. *Chemistry of Materials* **2008,** *20* (18), 5907-5915.
11. Jugović, D.; Uskoković, D., A review of recent developments in the synthesis procedures of lithium iron phosphate powders. *Journal of Power Sources* **2009,** *190* (2), 538-544.
12. Yoncheva, M.; Koleva, V.; Mladenov, M.; Sendova-Vassileva, M.; Nikolaeva-Dimitrova, M.; Stoyanova, R.; Zhecheva, E., Carbon-coated nano-sized LiFe1−x Mn x PO4 solid solutions ($0 \le x \le 1$) obtained from phosphate–formate precursors. *J Mater Sci* **2011,** *46* (22), 7082-7089.
13. Jensen, K. M. Ø.; Christensen, M.; Gunnlaugsson, H. P.; Lock, N.; Bøjesen, E. D.; Proffen, T.; Iversen, B. B., Defects in Hydrothermally Synthesized LiFePO4 and LiFe1-xMnxPO4 Cathode Materials. *Chemistry of Materials* **2013,** *25* (11), 2282-2290.
14. Huang, W.; Tao, S.; Zhou, J.; Si, C.; Chen, X.; Huang, W.; Jin, C.; Chu, W.; Song, L.; Wu, Z., Phase Separations in LiFe1–xMnxPO4: A Random Stack Model for Efficient Cathode Materials. *The Journal of Physical Chemistry C* **2013,** *118* (2), 796-803.
15. Zhou, X.; Wang, F.; Zhu, Y.; Liu, Z., Graphene modified LiFePO4 cathode materials for high power lithium ion batteries. *Journal of Materials Chemistry* **2011,** *21* (10), 3353-3358.
16. Amin, R.; Balaya, P.; Maier, J., Anisotropy of Electronic and Ionic Transport in LiFePO4 Single Crystals. *Electrochemical and Solid-State Letters* **2007,** *10* (1), A13-A16.
17. (a) Burba, C. M.; Frech, R., Raman and FTIR Spectroscopic Study of Li x FePO4 ($0 \leqslant x \leqslant 1$) *Journal of The Electrochemical Society* **2004,** *151* (7), A1032-A1038; (b) Yamada, A.; Takei, Y.; Koizumi, H.; Sonoyama, N.; Kanno, R.; Itoh, K.; Yonemura, M.; Kamiyama, T., Electrochemical, Magnetic, and Structural Investigation of the Lix(MnyFe1-y)PO4 Olivine Phases. *Chemistry of Materials* **2006,** *18* (3), 804-813.
18. Moore, P. B., Sarcopside: Its atomic arrangement. *American Mineralogist* **1972,** *57*, 24-35.
19. (a) Julien, C. M.; Mauger, A.; Ait-Salah, A.; Massot, M.; Gendron, F.; Zaghib, K., Nanoscopic scale studies of LiFePO4 as cathode material in lithium-ion batteries for HEV application. *Ionics* **2007,** *13* (6), 395-411; (b) Zaghib, K.; Ravet, N.; Mauger, A.; Gauthier, M.; Goodenough, J. B.; Julien, C., LiFePO4 High Electrochemical Performance at 60{degree sign}C with Purity Controlled by SQUID Magnetometry. *ECS Transactions* **2007,** *3* (27), 119-129.
20. Zaghib, K.; Mauger, A.; Gendron, F.; Julien, C. M., Magnetic studies of phospho-olivine electrodes in relation with their electrochemical performance in Li-ion batteries. *Solid State Ionics* **2008,** *179* (1–6), 16-23.
21. Bai, Y.; Yin, Y.; Yang, J.; Qing, C.; Zhang, W., Raman study of pure, C-coated and Co-doped LiFePO4: thermal effect and phase stability upon laser heating. *Journal of Raman Spectroscopy* **2011,** *42* (4), 831-838.
22. Paraguassu, W.; Freire, P. T. C.; Lemos, V.; Lala, S. M.; Montoro, L. A.; Rosolen, J. M., Phonon calculation on olivine-like LiMPO4 (M = Ni, Co, Fe) and Raman scattering of the iron-containing compound. *Journal of Raman Spectroscopy* **2005,** *36* (3), 213-220.
23. Julien, C. M.; Massot, M., Lattice vibrations of materials for lithium rechargeable batteries III. Lithium manganese oxides. *Materials Science and Engineering: B* **2003,** *100* (1), 69-78.
24. (a) Julien, C. M.; Gendron, F.; Amdouni, A.; Massot, M., Lattice vibrations of materials for lithium rechargeable batteries. VI: Ordered spinels. *Materials Science and Engineering: B* **2006,** *130* (1–3), 41-48; (b) Kim, T.-J.; Son, D.; Cho, J.; Park, B., Enhancement of the electrochemical properties of o-LiMnO2 cathodes at elevated temperature by lithium and fluorine additions. *Journal of Power Sources* **2006,** *154* (1), 268-272.
25. Zhang, L.; Brow, R. K., A Raman Study of Iron–Phosphate Crystalline Compounds and Glasses. *Journal of the American Ceramic Society* **2011,** *94* (9), 3123-3130.

26. Qin, X.; Wang, J.; Xie, J.; Li, F.; Wen, L.; Wang, X., Hydrothermally synthesized LiFePO4 crystals with enhanced electrochemical properties: simultaneous suppression of crystal growth along [010] and antisite defect formation. *Physical Chemistry Chemical Physics* **2012,** *14* (8), 2669-2677.
27. Bini, M.; Mozzati, M. C.; Galinetto, P.; Capsoni, D.; Ferrari, S.; Grandi, M. S.; Massarotti, V., Structural, spectroscopic and magnetic investigation of the LiFe1−xMnxPO4 (x=0–0.18) solid solution. *Journal of Solid State Chemistry* **2009,** *182* (7), 1972-1981.
28. Lee, M. H.; Kim, T. H.; Kim, Y. S.; Song, H. K., Precipitation Revisited: Shape Control of LiFePO4 Nanoparticles by Combinatorial Precipitation. *J Phys Chem C* **2011,** *115* (25), 12255-12259.

Figure Captions:

Fig.1: Field emission scanning electron micrograph of $LiFe_{1-x}Mn_xPO_4$ (a) $x = 0$, (b) $x = 0.05$, (c) $x = 0.10$, (d) $x = 0.25$.

Fig.2: (a) X-ray diffraction pattern of (x = 0, 0.05, 0.10, 0.25). (b) The unit cell volume as a function of Mn concentration (x).

Fig.3: (a) Magnetization as a function of magnetic field, (b) Inverse magnetic susceptibility *vs* Temperature plots, (c) magnified plot of figure (b) in the low temperature regime, and (d) the change in μ_{eff} and Neel temperature as a function of Mn (x = 0 to 0.25) of $LiFe_{1-x}Mn_xPO_4$.

Fig. 4: Raman spectra of $LiFe_{1-x}Mn_xPO_4$ (x = 0, 0.05, 0.10, 0.25). (a) in the 100 to 800 cm^{-1} range, (b) in the 800 to 1300 cm^{-1} range, and (c) the peak fit for the Raman spectra in the 350 to 700 cm^{-1}.The peaks marked with # corresponds to $Fe_3(PO_4)_2$/ $Mn_3(PO_4)_2$/$(Fe_{1-x}Mn_x)_3PO_4$ and * corresponds to Li-Mn-O phases.

Fig. 5: FTIR spectra of $LiFe_{1-x}Mn_xPO_4$ (x = 0, 0.05, 0.10, 0.25). (a) in the 400 to 1300 cm^{-1} range, (b) the peak fit for the FTIR spectra in the 800 to 1200 cm^{-1} , (c) The deconvoluted peak position of ν_1 absorption mode in b as a function of 'x'

Fig.6: (a) Bright-field TEM image and (b) high resolution transmission electron microscopy (HRTEM) image of $LiFe_{1-x}Mn_xPO_4$ with x=0.05 sample (c) The elemental mapping of Fe, Mn, O and P from the region shown in STEM image is shown.

Fig.7: (a) Bright-field TEM image and (b) high resolution transmission electron microscopy (HRTEM) image of $LiFe_{1-x}Mn_xPO_4$ with x=0.25 sample. The inset in (b) shows the SAD pattern from the crystallite. (c) STEM-EDS line-profile and (d) the elemental mapping of Fe, Mn, O and P of the crystal from the region marked by the black line in STEM image.

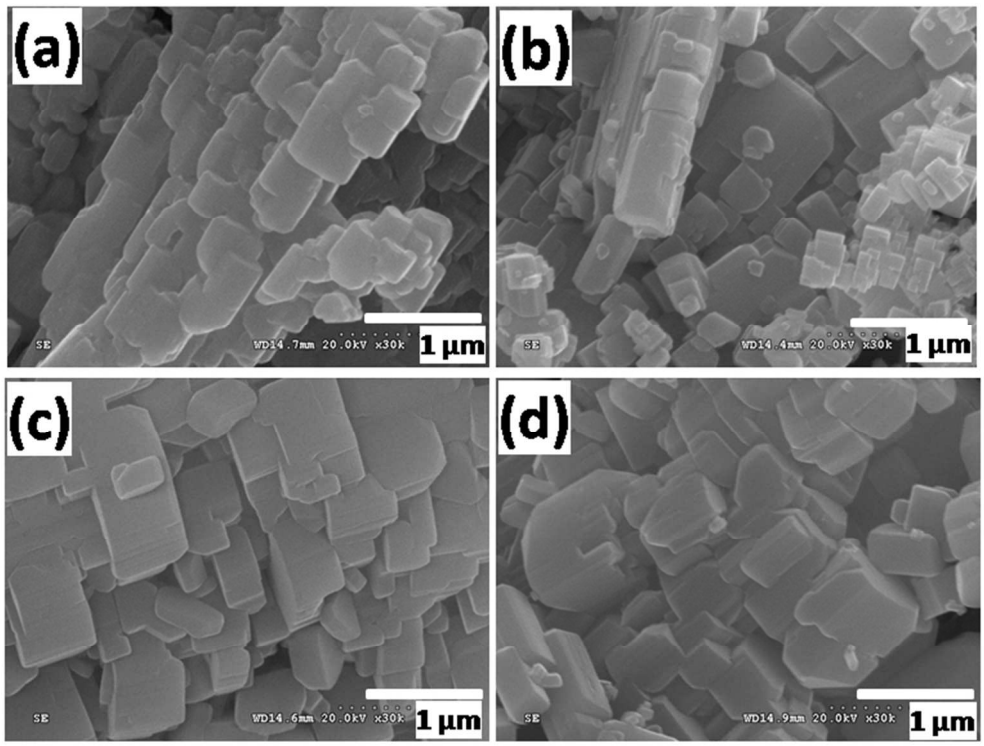

164x123mm (120 x 120 DPI)

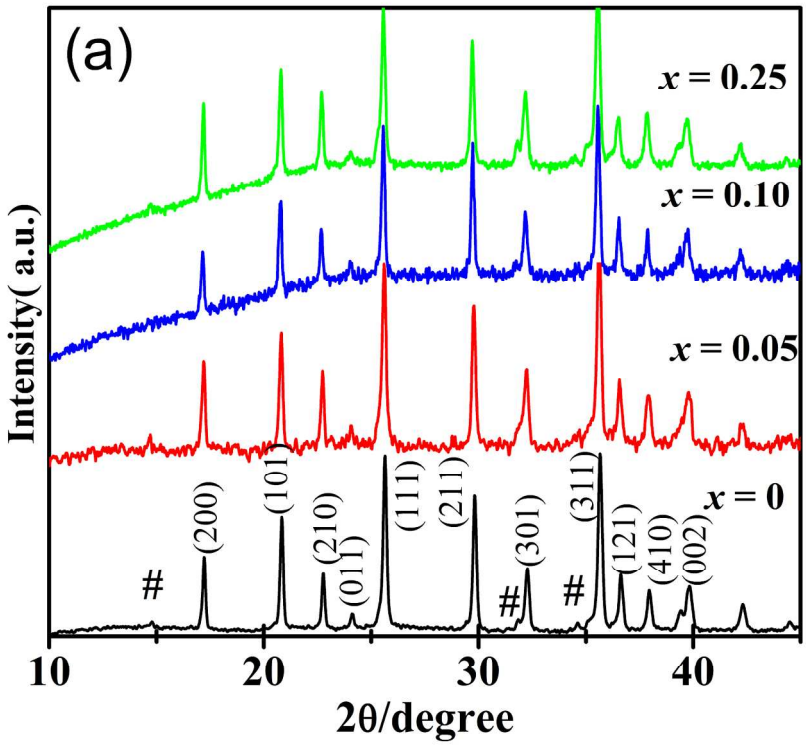

423x325mm (120 x 120 DPI)

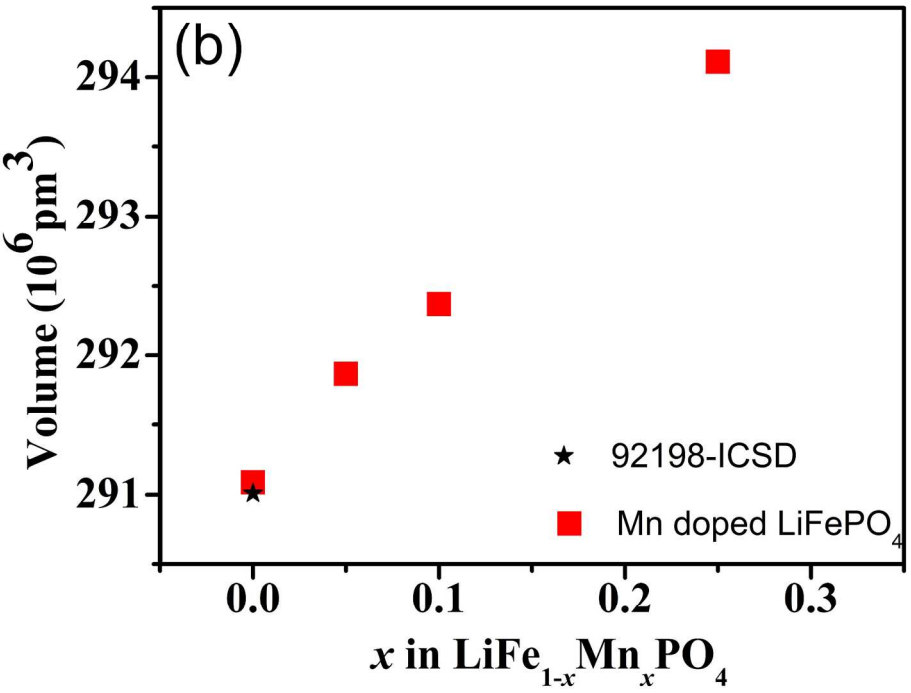

423x324mm (120 x 120 DPI)

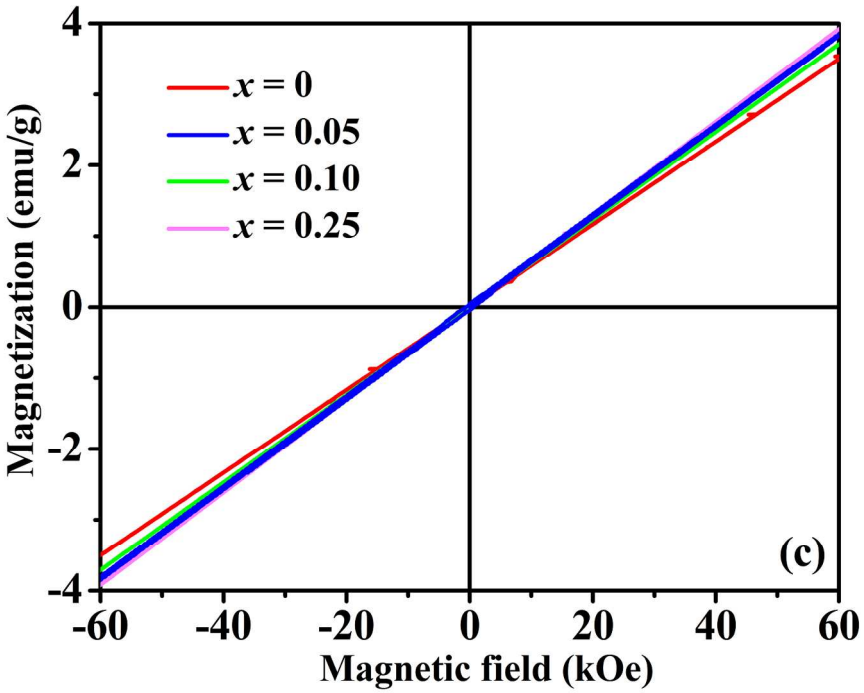

423x324mm (120 x 120 DPI)

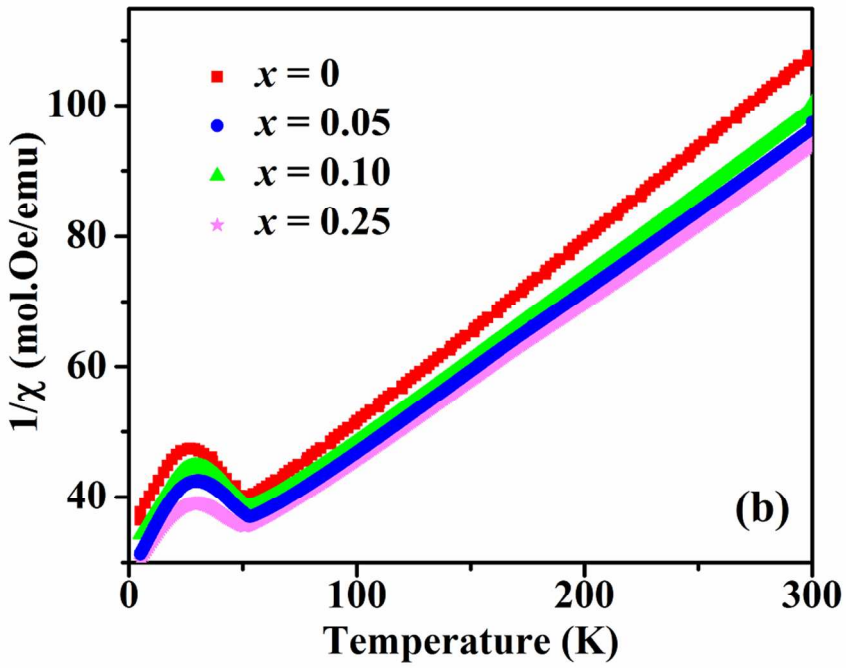

101x78mm (300 x 300 DPI)

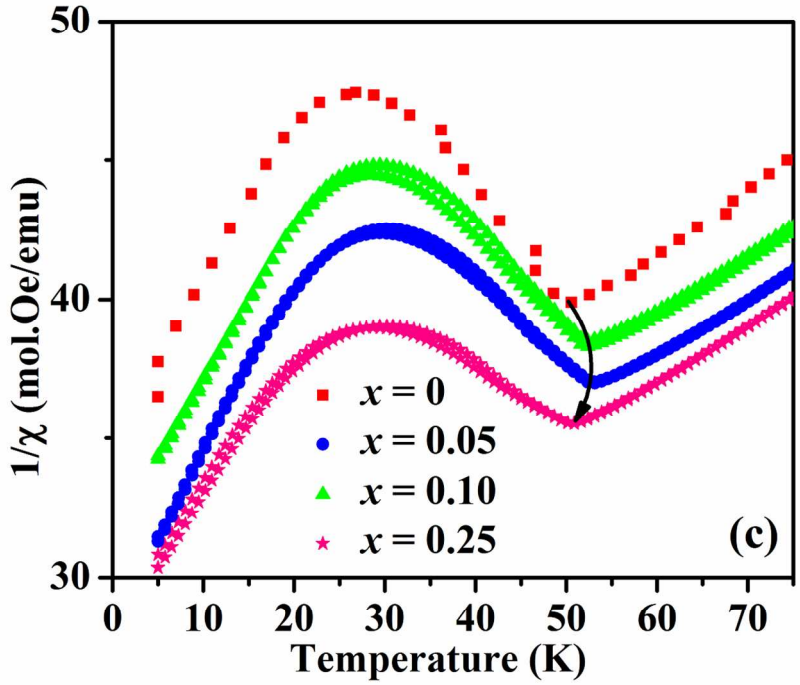

127x98mm (300 x 300 DPI)

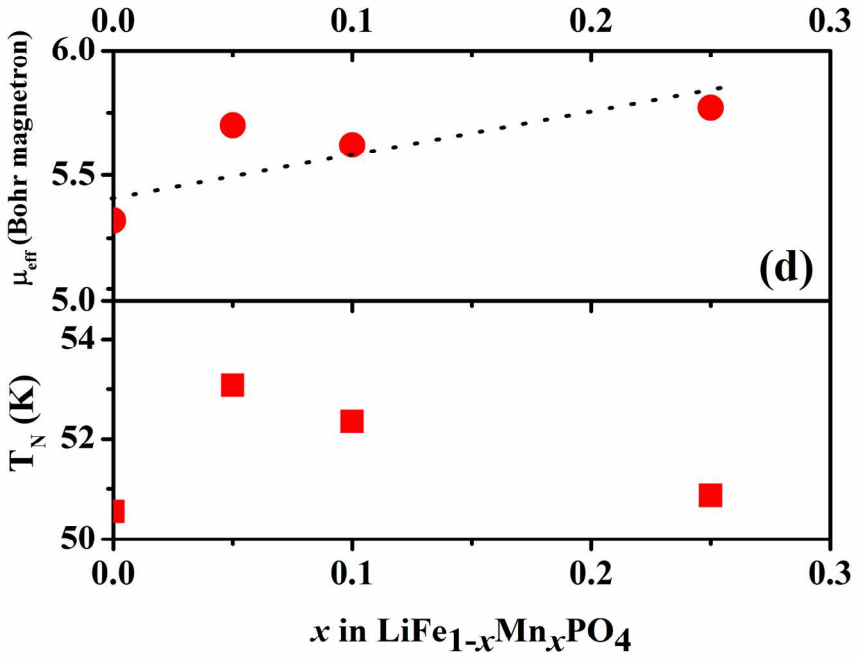

169x130mm (300 x 300 DPI)

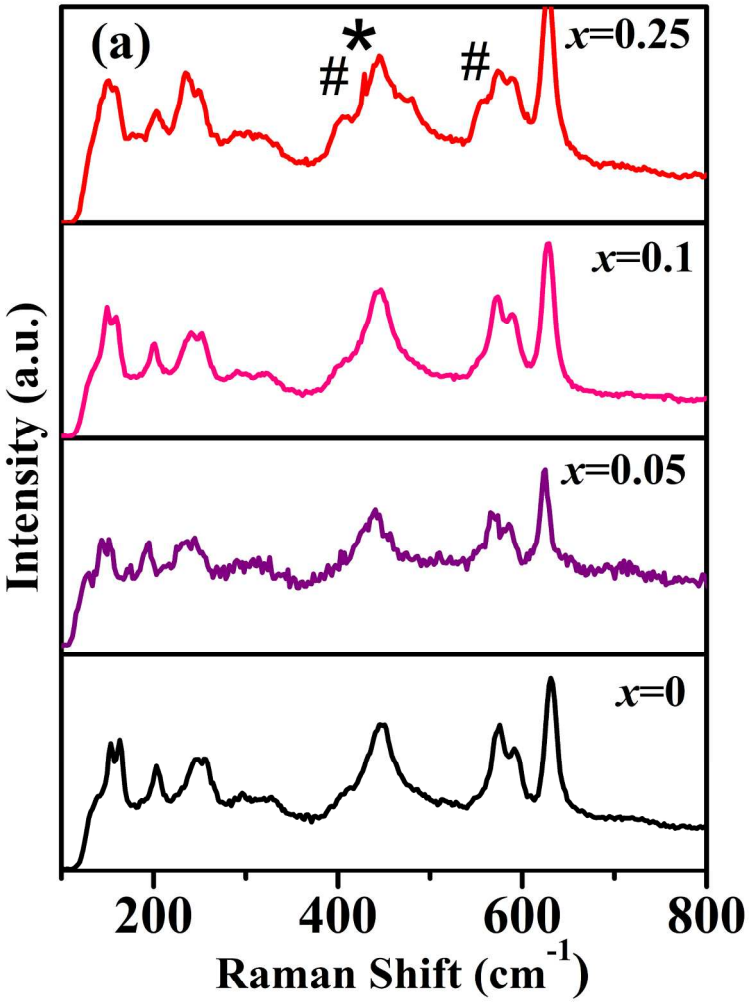

423x551mm (120 x 120 DPI)

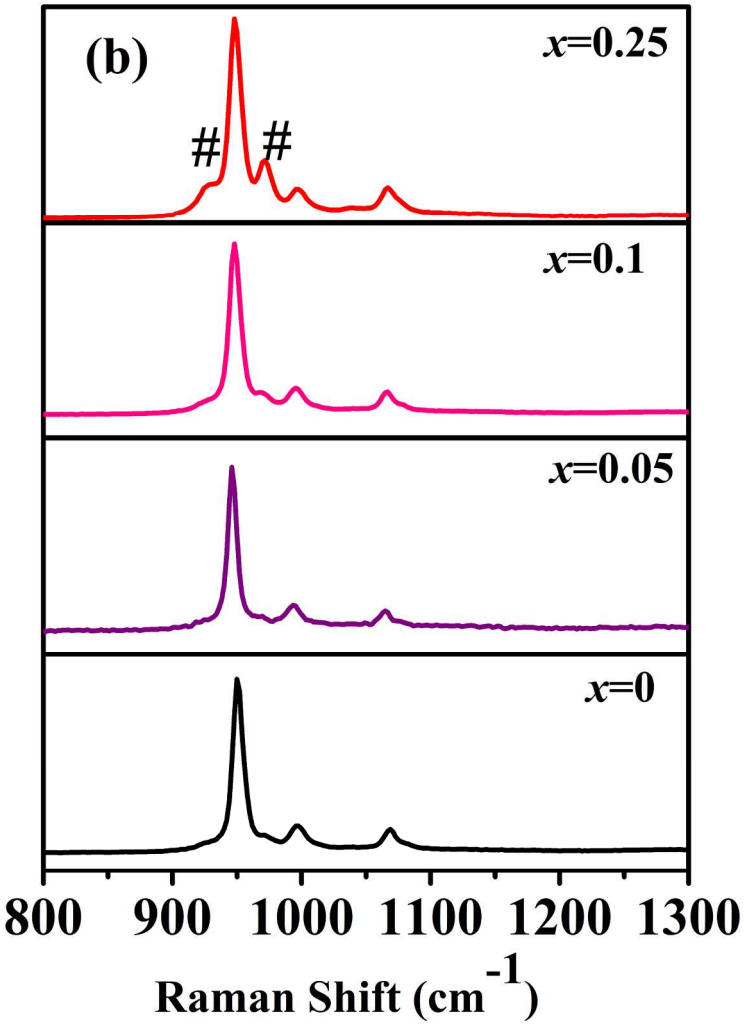

423x551mm (120 x 120 DPI)

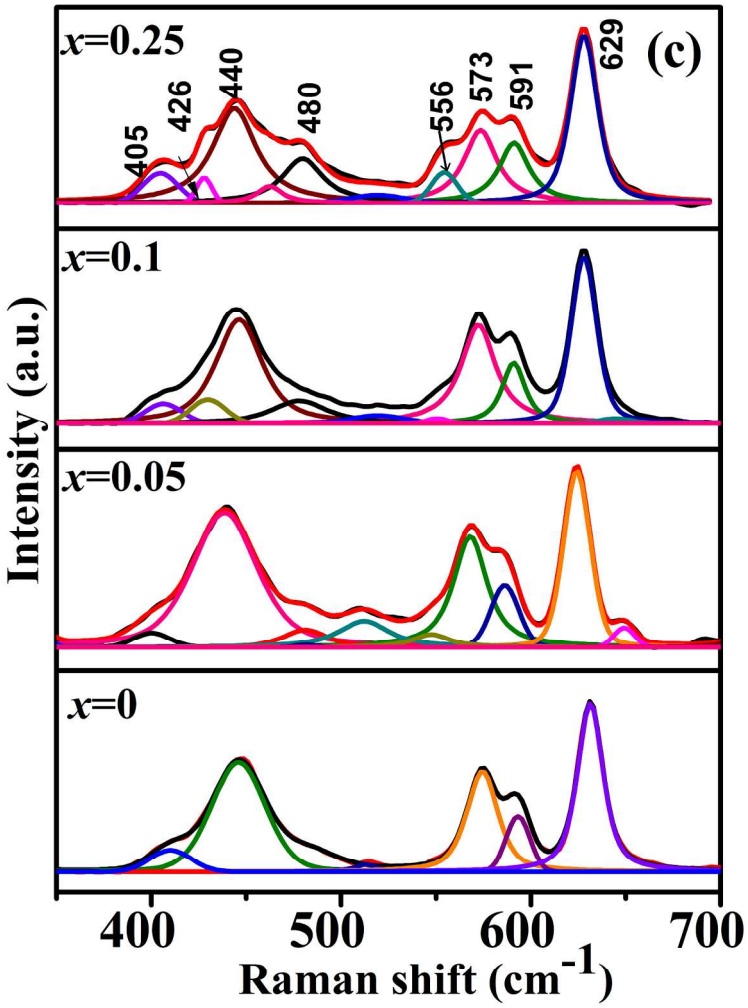

423x552mm (120 x 120 DPI)

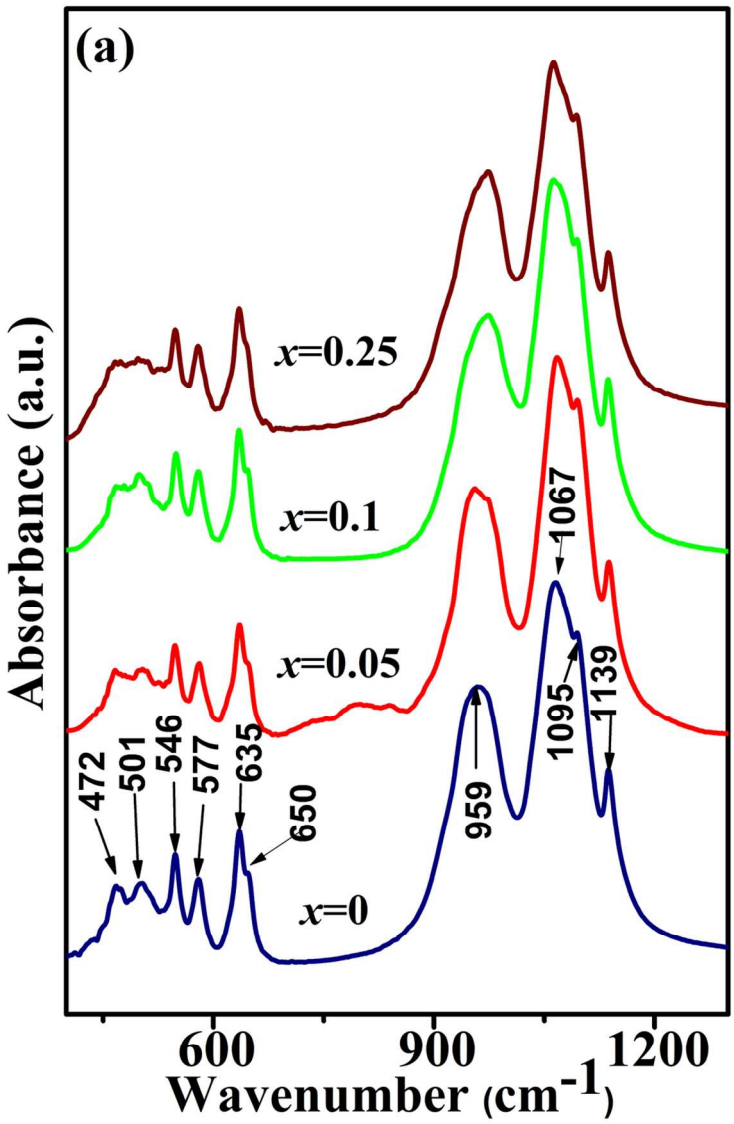

110x144mm (300 x 300 DPI)

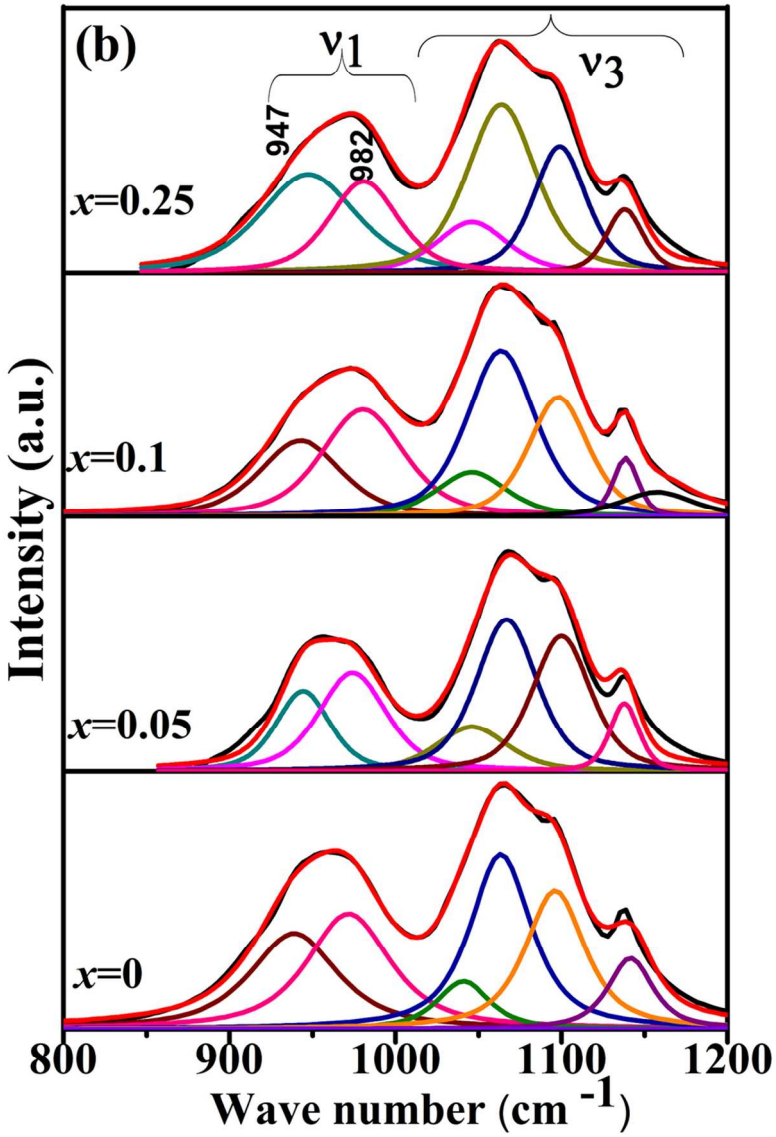

99x129mm (300 x 300 DPI)

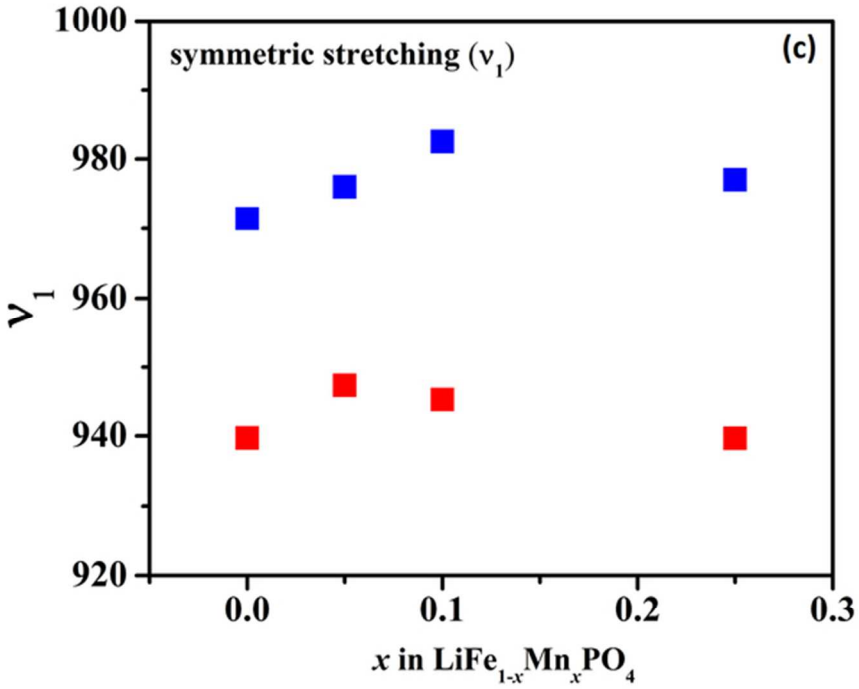

58x45mm (300 x 300 DPI)

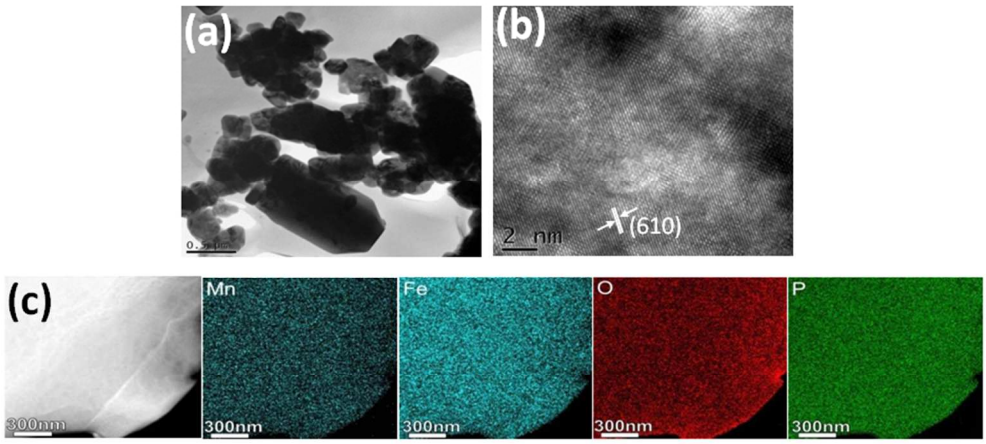

200x97mm (120 x 120 DPI)

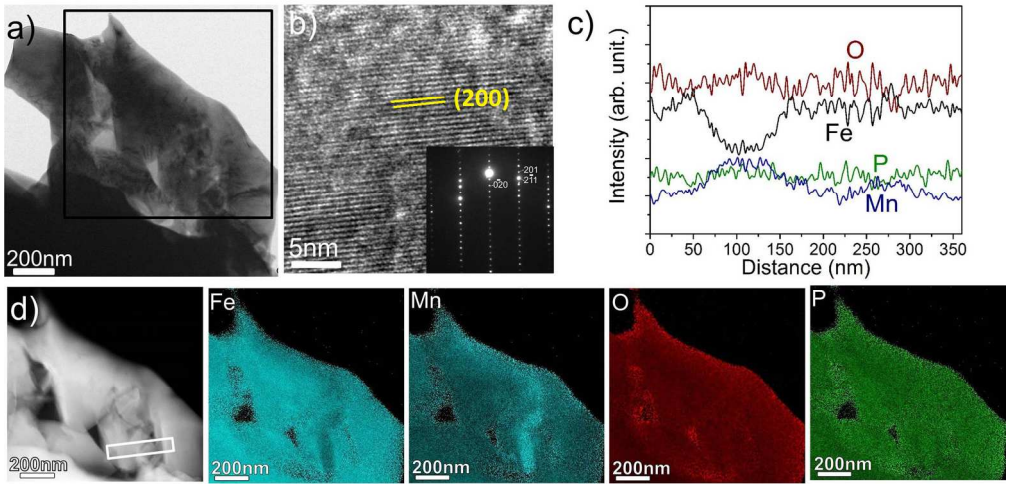

381x184mm (150 x 150 DPI)